Originally published as:

A link between reduced Barents-Kara sea ice and cold winter extremes over northern continents

Vladimir Petoukhov[1] and Vladimir A. Semenov[2,3]

[1]   The recent overall Northern Hemisphere warming was accompanied by several severe northern continental winters, as for example, extremely cold winter 2005–2006 in Europe and northern Asia. Here we show that anomalous decrease of wintertime sea ice concentration in the Barents-Kara (B-K) seas could bring about extreme cold events like winter 2005–2006. Our simulations with the ECHAM5 general circulation model demonstrate that lower-troposphere heating over the B-K seas in the Eastern Arctic caused by the sea ice reduction may result in strong anticyclonic anomaly over the Polar Ocean and anomalous easterly advection over northern continents. This causes a continental-scale winter cooling reaching $-1.5°C$, with more than 3 times increased probability of cold winter extremes over large areas including Europe. Our results imply that several recent severe winters do not conflict the global warming picture but rather supplement it, being in qualitative agreement with the simulated large-scale atmospheric circulation realignment. Furthermore, our results suggest that high-latitude atmospheric circulation response to the B-K sea ice decrease is highly nonlinear and characterized by transition from anomalous cyclonic circulation to anticyclonic one and then back again to cyclonic type of circulation as the B-K sea ice concentration gradually reduces from 100% to ice free conditions. We present a conceptual model that may explain the nonlinear local atmospheric response in the B-K seas region by counter play between convection over the surface heat source and baroclinic effect due to modified temperature gradients in the vicinity of the heating area.

1. Introduction

[2] In the recent decades, the strongest warming during the winter half of the year was observed in the Arctic, exceeding by a factor of two hemispheric mean changes [*Polyakov et al.*, 2002; *Serreze and Francis*, 2006]. The wintertime Arctic warming was accompanied by a rapid decrease in sea ice cover [*Parkinson et al.*, 1999; *Stroeve et al.*, 2007]. Ongoing global warming has also brought noticeably milder winters to the northern extratropics, in particular, to Europe [*Philipona et al.*, 2005]. Yet a number of extremely cold northern continental winters have occurred during the period of overall warming trend and sea ice decline. One recent example is anomalously cold winter 2005–2006 over northern parts of the continents in the Northern Hemisphere (NH). In January 2006, monthly mean surface air temperature (SAT) anomalies according to National Center for Environmental Prediction/National Center for Atmospheric Research (NCEP/NCAR) reanalysis data [*Kalnay et al.*, 1996] reached $-4°C$ in Europe and $-10°C$ in central Siberia (Figure 1a) which is quite comparable with a transition from present day climate to the Last Glacial Maximum climate conditions [*Calov et al.*, 2005a, 2005b]. Interestingly, cold anomalies over Eurasia were accompanied by extremely high Arctic temperatures, exceeding by more than $14°C$ climatological means (Figure 1a). The winter 2005–2006 was marked neither by anomalously low North Atlantic Oscillation (NAO) index usually associated with negative temperature anomalies over Europe and Siberia [*Hurrell*, 1995] nor was there an El Niño event [*Diaz and Markgraf*, 2000], also found to bring about cold extremes over Europe [*Fraedrich and Müller*, 1992; *Merkel and Latif*, 2002; *Brönnimann et al.*, 2004] (see, e.g., the time series of the atmospheric circulation indices at Climate Prediction Center of the NOAA/National Weather Service [*NOAA*, 2010]).

[3] The exceptionally cold temperatures over northern land areas in winter 2005–2006 went alone with positive anomalies of the North Atlantic and Tropical Ocean sea surface temperatures (SSTs), as well as the NH average SAT. In that sense, the winter 2005–2006 phenomenon might be thought of as a random weather event. On the other hand, it persisted over the whole winter and was of a con-

---

[1]Potsdam Institute for Climate Impact Research, Potsdam, Germany.
[2]Leibniz Institute of Marine Sciences at the University of Kiel, Germany.
[3]A.M. Obukhov Institute of Atmospheric Physics RAS, Moscow, Russia.
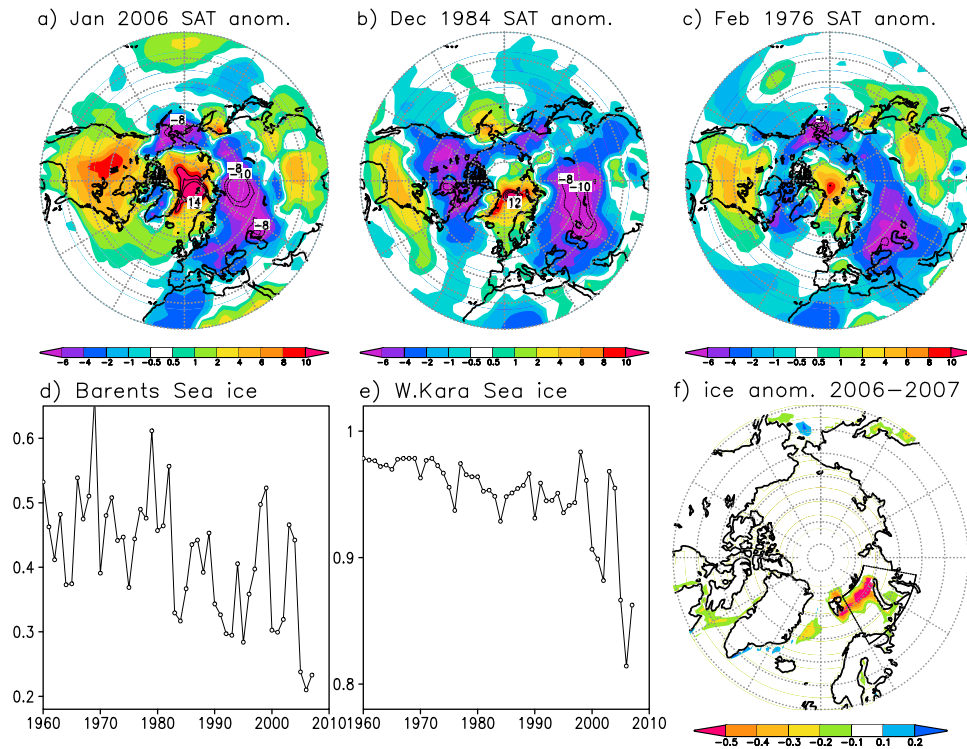
Figure 1. Observed winters with cold continental temperatures contrasting warm Arctic and negative sea ice anomalies in the Barents and Kara seas. SAT anomalies (in °C) relative to the 1948–2006 mean for (a) January 2006, (b) December 1984, and (c) February 1976. Time series of the mean sea ice concentration (as a fraction of one) for December–January–February (DJF) in (d) the Barents Sea (30°E–60°E, 70°N–80°N) and (e) the western Kara Sea (60°E–80°E, 70°N–80°N); (f) DJF sea ice concentration anomalies (as a fraction of one) averaged over the years 2006 and 2007 relative to the (1981–2000) mean; the marked 30°E–60°E/65°N–80°N sector is the area, where the sea ice concentration was modified for November through April in the six ECHAM5 simulations.

tinental scale. Case studies of this exceptional event reveal a specific "blocking-like" circulation pattern, which might have been favored by warm SST anomalies in the northern North Atlantic [*Croci-Maspoli and Davies*, 2009] with indications for important role of troposphere-stratosphere interactions [*Scaife and Knight*, 2008]. Circulation anomalies linked to stratospheric warming may descend into the troposphere leading to weak NAO (AO) and associated cooling over Eurasia [*Baldwin and Dunkerton*, 2001]. The stratosphere warming events, in turn, may be triggered by enhanced planetary waves in the previous fall related to anomalous troposphere circulation or boundary forcing, such as snow cover or sea ice [*Takaya and Nakamura*, 2005, 2008; *Cohen et al.*, 2007; *Honda et al.*, 2009]. This latter mechanism involves delayed (by 2–3 months) dynamical response implying importance of lower boundary forcing in autumn for the following winter conditions.

[4] Several modeling studies have reported on significant impact of altered Arctic sea ice conditions on atmospheric circulation [*Herman and Johnson*, 1978; *Bengtsson et al.*, 2004; *Magnusdottir et al.*, 2004; *Deser et al.*, 2004; *Alexander et al.*, 2004; *Singarayer et al.*, 2006; *Seierstad and Bader*, 2009]. In the study by *Alexander et al.* [2004], the local circulation response was baroclinic and resulted in rather shallow near-surface warming, whereas the associated large-scale circulation realignment was of barotropic struc-ture. Feedback of ice changes upon circulation was positive (negative) in the Pacific (Atlantic) sectors. Similar results have been obtained by *Magnusdottir et al.* [2004] and *Deser et al.* [2004].

[5] Here, we highlight that the cold winter 2005–2006 coincided with the lowest recorded, to that time, December–January–February sea ice extent in the Barents and Kara (B-K) seas in the eastern opening of the Arctic Ocean (Figures 1d and 1e). It was the first year since the satellite observations era, when the western part of the Kara Sea was free of ice in winter months, and the sea ice cover in both seas was unprecedentedly low [*Cavalieri et al.*, 1996].

[6] The wintertime SAT 2005–2006 warming in the Eastern Arctic was linked to increased heat losses from the ice-free sea surface, exposed to the cold and windy Arctic atmosphere. This is indicated by location of the strongest positive SAT anomaly over the area of major sea ice changes (Figures 1a and 1f). We note that the pattern of cold northern continents contrasting warm Arctic was not unique for winter 2005–2006. For example, two similar cold events have occurred in December 1984 and February 1976 (shown in Figures 1b and 1c), as well as several others, e.g., in December 1966, December 1969, and February 1984 (not shown). These events also featured low B-K sea ice cover and exhibited large-scale SAT anomaly patterns that are rather similar to those shown in Figures 1a–1c. Yet the
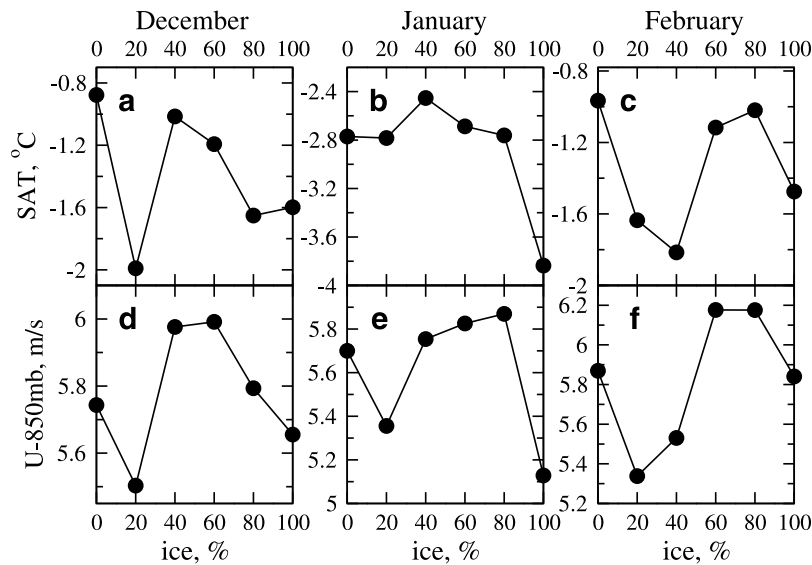
Figure 2. Simulated in the ECHAM5 experiments (a–c) monthly SAT (in °C) and (d–f) zonal wind at 850 hPa (in m/s) over the European region (10°E–30°E, 45°N–55°N) as functions of prescribed sea ice concentrations (in %) in the Barents-Kara seas for (a and d) December, (b and e) January, and (c and f) February. SAT changes exceeding 0.59°C, 0.61°C, and 0.52°C are statistically significant at (at least) 90% confidence level for December, January, and February, respectively.

NAO, AO, and Southern Oscillation Index indices in those months did not imply a characteristic SAT cooling [*Osborn*, 2006; *NOAA*, 2010]. This suggests an important role of the anomalous (reduced) sea ice conditions in triggering indicated cold winter extremes over northern continents.

[7] We suggest that heating of the lower troposphere over the B-K seas may cause a decreased meridional temperature gradient in subarctic latitudes bringing about changes of atmospheric circulation with possible weakening of zonal winds in midlatitudes (that was the case, in particular, for the winter 2005–2006). This can initiate cooling of the northern continental areas. To elaborate on this idea, we analyzed a sensitivity of wintertime atmospheric circulation in the extratropics to sea ice concentration in the B-K seas (ranging from 1% through 100%) in a series of simulations with atmospheric general circulation model European Centre/Hamburg (ECHAM5) [*Roeckner et al.*, 2003].

2. Atmospheric Model and Simulation Setup

[8] The ECHAM5 is the latest version of the ECHAM atmospheric general circulation model developed at the Max Planck Institute for Meteorology. It is a spectral model employing state-of-the-art physics. A detailed description of the model is given in the study by *Roeckner et al.* [2003]. The version used for our simulations has T42 horizontal spectral resolution (approximately 2.8° × 2.8° longitude/latitude) and 19 vertical levels.

[9] We performed six simulations with the ECHAM5 model. All simulations were of 100 years duration and used prescribed lower boundary conditions (repeating annual cycle of sea surface temperatures and sea ice concentrations). Sea surface temperatures (SSTs) were the same for all six simulations. Specifically, taken from Atmospheric Model Intercomparison Project II data set [*Hurrell et al.*, 2008], SSTs for September–December were set as in the

year 2005, and for January to May as in the year 2006, to represent the global SST evolution during the boreal cold season 2005–2006. SSTs for June through August were prescribed as average for the years 2005 and 2006. Sea ice concentration in all six simulations was assigned to the 1987–2006 climatological mean data [*Hurrell et al.*, 2008] everywhere except for the Barents-Kara (B-K) sector (30°E–80°E, 65°N–80°N, see Figure 1f). Sea ice concentration in this sector (hereafter referred to as SIC) in May through October was assigned to the 1987–2006 climatology [*Hurrell et al.*, 2008] in all six simulations, whereas November through April SIC was set to six different constant values, namely, 100%, 80%, 60%, 40%, 20%, and 1% in six corresponding simulations. The model prescribed −1.8°C (mean freezing temperature) to the open water SST in the grid cells within the B-K sector partially covered by ice.

3. Results

[10] The results discussed below present 100 year averages obtained from the described above six ECHAM5 simulations.

3.1. Nonlinearity of SAT and Lower Troposphere Circulation Response to SIC Reduction

[11] Model runs reveal rather pronounced nonlinear response of surface air temperatures and zonal winds (illustrated here by zonal wind in the lower free troposphere at 850 hPa, U_{850}) to the imposed changes of SIC in winter months. Strongly linked responses of the SAT and U_{850} are illustrated by 100 year means over Europe (Figure 2). The European sector (10°E–30°E, 45°N–44°N) is located in the area of the strongest cooling anomaly simulated by the model for February when SIC reduces from 80% to 40% (see Figure 3b and discussion below) and covers the most densely populated area in the northern Eurasia. Observational results (see Figure 1a) also suggest that Europe was
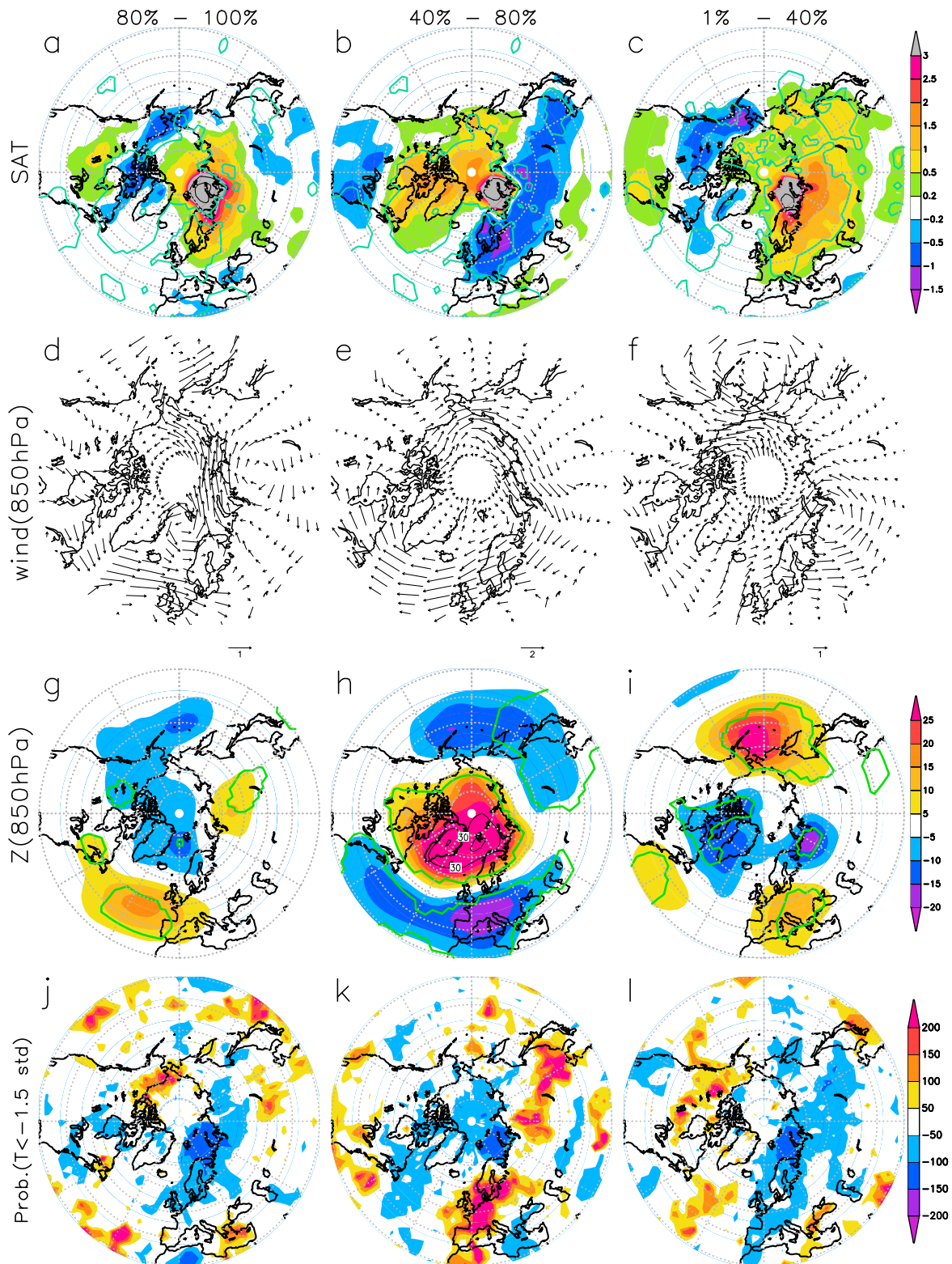
Figure 3. Simulated with ECHAM5 monthly SAT and the low-troposphere circulation responses to decrease in the Barents-Kara sea ice concentration (SIC) from 100% to 80%, 80% to 40%, and 40% to 1% for February. Differences between SAT (in °C) simulated with SIC change from (a) 100% to 80%, (b) 80% to 40%, and (c) 40% to 1%; (d–f) same as Figures 3a–3c but for the vector of the horizontal wind at 850 hPa (in m/s); (g–i) same as Figures 3a–3c but for the geopotential height at 850 hPa (Z_{850}, in gpm); (j–l) same as Figures 3a–3c but for probabilities (in %) for the February SAT to be less than −1.5 standard deviation. The reference probabilities in all cases correspond to higher SIC. Thick green contour lines encompass SAT and Z_{850} anomalies that are statistically significant at 90% confidence level.

among the regions (alone with the northern Asia) most strongly affected by the winter 2005–2006 frosts. As shown in Figure 2, warming and strengthening of U_{850} take place when SIC reduces from 100% to 80%, particularly pronounced in January and February. Further decrease in SIC from 80% to 60% for February (or from 80% to 40% for January or 60% to 40% for December) is not accompanied by noticeable changes in SAT and U_{850}. In contrast, sharp cooling and weakening of U_{850} occur in the model when SIC is reduced to 40% for February (or to 20% for December and January). Further SIC reduction to 1% causes relative warming and corresponding increase in U_{850}. A Student's t test on the significance of the SAT and U_{850} differences between different simulations depicted in Figure 2 indicates that the nonlinear dependence of the SAT changes on gradual SIC reduction in December and February is statistically significant at (at least) 90% confidence level (see the figure caption for the values of significant differences). Considerable continental cooling under SIC reduction from high to moderate values indicates that the cold winters like the 2005–2006 event might have been favored by anomalous heating in this sector of the Arctic.

[12] To get insight into the links between changes in temperature and atmospheric circulation, we analyze geographical patterns of their response to SIC decrease in different simulations for February, which serves as a good illustration of the nonlinear S-shaped dependence of European SAT and U_{850} on monotonic sea ice decrease. Figures 3a–3c show changes in SAT, Figures 3d–3f show changes in lower troposphere (850 hPa) atmospheric wind, and Figures 3g–3i show changes in geopotential height caused by SIC decrease from 100% to 80% (Figures 3a, 3d, and 3g), 80% to 40% (Figures 3b, 3e, and 3h), and 40% to 1% (Figures 3c, 3f, and 3i). These three SIC differences are chosen as they correspond to the transitions between extremes of the SAT curve in Figure 2c (warming, cooling, and warming again as SIC gradually decreases). We would like to emphasize that the only difference in boundary conditions in the simulations presented in Figure 3 is SIC in the B-K sector (Figure 1f) that is uniformly altered. The SIC changes are indicated over the columns. Note a strong warming over the B-K sector with sharp gradients at its border that is seen in Figure 3 for all three cases of SIC decrease.

[13] Comparison of the SAT and wind changes in Figure 3 reveals a reason for particularly good correspondence between temperature and zonal wind changes over Europe in February shown in Figure 2. Anomalous north-westerlies, bringing warm Atlantic air in cases of (1%–40%) and (80%–100%) SIC changes, are contrasted by strong anomalous easterly flow over this region for (40%–80%) SIC difference. The latter is also a distinctive feature of the extreme European winter 2005–2006 event accompanied by the anomalous north-easterly and strong cooling over the European site according to NCEP/NCAR reanalysis data [*Kalnay et al.*, 1996].

3.2. SAT and Lower Troposphere Circulation Response to SIC Reduction From 80% to 40%

[14] Simulated pattern of SAT response to SIC decrease from 80% to 40% (Figure 3b) is drastically different to the changes in SAT associated with 100% to 80% and 40% to 1% SIC reduction (Figures 3a and 3c). This pattern has very

much in common with the observed SAT anomaly in winter 2005–2006 (Figure 1a). Strong warming over the B-K seas (that is general for all three SIC transitions) is contrasted by considerable cooling in adjacent northern Eurasia. The cold SAT anomaly reaching −1.5°C extends over the continent from Western Europe through the Western Siberia to Southern China. Negative SAT anomalies, although of smaller magnitude, also cover a large part of North America (Figure 3b). Major SAT anomalies are statistically significant as indicated by green contours in Figure 3 (note a particularly large area of significant changes over European sector and in the northeastern Asia). The SAT changes are readily explained by near-surface wind changes. Strong anomalous easterlies dominate the circulation response in the lower troposphere to SIC decrease from 80% to 40% for almost the whole 45°N–70°N latitudinal band (Figure 3e) thereby reducing westerly flow. The wind differences match well the associated changes of Z_{850} geopotential, with maximum anomaly of 35 gpm over central Arctic (Figure 3h), which are highly statistically significant. This implies a strong anticyclonic anomaly over the high Arctic with a center over the Barents Sea. Such a response is very interesting as one would rather expect a cyclonic anomaly over the surface heat source and a warming over adjacent territories.

[15] A spatial map of December SAT changes (that also exhibit nonlinear features) for the anomalous cooling as SIC reduces to 20% (not shown) looks rather similar to the February response shown in Figure 3.

3.3. SAT and Lower Troposphere Response to SIC Change From 100% to 80% and 40% to 1%

[16] Simulated patterns of SAT response to SIC reduction from 100% to 80% and from 40% to 1% (Figures 3a and 3c, respectively) are quite similar exhibiting a rather symmetrical warming around the heating area. Circulation changes in these cases (Figures 3d and 3g and Figures 3f and 3i, accordingly) are also closely linked to the corresponding changes in SAT. Unlike the 80% to 40% SIC decrease that sets up the anticyclonic anomaly over central Arctic (Figures 3e and 3h), both 100% to 80% and 40% to 1% reductions of SIC bring about cyclonic tendencies in polar latitudes (Figures 3d and 3g and Figures 3f and 3i). In case of 100% to 80% SIC decrease (Figures 3d and 3g), a strong cyclone-type circulation to the northwest of the Barents Sea is accompanied by an anticyclone vortex in the central northern Siberia. In spite of more pronounced warming over the B-K seas caused by 100% to 80% SIC decrease, as compared to that for 40% to 1% SIC reduction (compare Figures 3a and 3c), the rearrangement of the atmospheric circulation is more prominent in the latter case (compare Figures 3d and 3g and Figures 3f and 3i). It is manifested by two cyclonic minima around the southern cost of the Barents Sea and next to Canadian Archipelago (Figures 3f and 3i). In addition, a strong anticyclonic circulation develops in that case just south of the Bering Strait that transports warmer Pacific air masses to the Far East. This shapes an overall warming encompassing basically the whole Eurasia.

3.4. Comparison With Canonical NAO and AO Patterns

[17] Although the SAT changes shown in Figures 3a–3c resemble those associated with positive (Figures 3a and

3c) and negative (Figure 3b) extremes of the NAO [*Hurrell*, 1995], there are several important differences. Specifically, in Figure 3b, the anomalous cooling over Eurasia is accompanied by a hot temperature spot over the B-K seas, whereas the low NAO phase is characterized by sea ice increase and cooling in that region [*Hurrell*, 1995; *Dickson et al.*, 2000]. The corresponding anomalous Z_{850} pattern in Figure 3h is reminiscent of the negative phase of the Arctic Oscillation (AO) or Northern annular mode [*Thompson and Wallace*, 1998] but differs in key features. A principally important shift of the anomalous high-latitude blocking-like structure from the subpolar North Atlantic/Western Arctic to Eastern Arctic is clearly seen in Figure 3h. The shift is accompanied with the corresponding counterclockwise turn of the whole structure around the pole, which brings about stronger easterly anomaly (and hence, more pronounced cooling) over the northern Eurasia, as compared to the classical negative NAO. Unlike the canonical AO, the physical reason for the considered pattern (Figure 3h) is not a modulation in the strength of the polar vortex aloft [*Thompson and Wallace*, 1998] but rather the anomalous surface heat source in the B-K sector, which triggers the development of the local blocking-like structure in the lower troposphere above the B-K sector in case of 80% to 40% SIC reduction. This local anomalous structure serves as the primary pacemaker, in the sense of the spatial phase, for an overall atmospheric circulation realignment shown in Figures 3e and 3h. This idea is supported by anomalous atmospheric circulation patterns for the cases of 100% to 80% and 40% to 1% SIC decrease shown in Figures 3d and 3g and Figures 3f and 3i, respectively. A noticeable shift of the southernmost edge of the cyclone-type structure from the subpolar North Atlantic/Western Arctic to Eastern Arctic is observed in these figures as compared to the case of the positive NAO.

3.5. Vertical Structure of Troposphere and Lower Stratosphere Circulation Responses to SIC Reduction

[18] The patterns of geopotential height anomalies through the troposphere (Figure 4) principally differ from the corresponding anomalies associated with the negative NAO, in case of 80% to 40% SIC decrease (Figures 4b, 4e, and 4h) and from the positive NAO, in the events of 100% to 80% (Figures 4a, 4d, and 4g) and 40% to 1% (Figures 4c, 4f, and 4i) SIC reduction.

[19] Figures 4b, 4e, and 4h demonstrate, in particular, the aforementioned counterclockwise turn of the anomalous blocking-like structure around the pole as compared to the canonic negative NAO pattern. The positive anomaly expands far deep to the south with increase in height. At the same time, both 100% to 80% and 40% to 1% SIC transitions trigger a development of the anomalous atmospheric circulation structures turned, relative to the positive-NAO structure, counterclockwise around the pole in the lower and middle troposphere (compare Figures 4a and 4d and Figures 4c and 4f). This is due to the lower-troposphere heat anomaly in the B-K sector as a source of the indicated anomalous atmospheric circulation structures. In the upper troposphere and lower stratosphere, a spatial pattern of the geopotential height anomaly still resembles the counterclockwise-turned positive NAO pattern in the case of 40% to 1% SIC decrease (Figures 4i and 4l). Meanwhile, unlike the positive NAO structure, the

anomalous Z_{250} and Z_{100} patterns for the 100% to 80% SIC decrease are practically in the opposite spatial phase to their counterparts in the lower- and middle-troposphere over the Barents Sea Region (compare Figures 4a and 4g).

3.6. Changes in Probabilities of Extreme Cold Events

[20] The cold continental SAT anomaly (Figure 3b) represents a mean (averaged over 100 years of integration) climatic response simulated by the model and cannot completely explain the observed extremely cool temperatures in particular years (e.g., in winter 2005–2006), being some 2–3 times weaker. However, this mean response is accompanied by a modification of the probability distribution function, which may lead to a noticeable increase in probability of extreme events. Simulated changes of probability for negative SAT anomalies to be colder than 1.5 standard deviations are much stronger than the mean SAT response, for all three considered cases of SIC reduction (Figures 3j–3l). Importantly, the 80% to 40% SIC decrease is marked by a very strong increase in cold extreme probabilities exceeding 200% over large areas in Europe, central Siberia, and China (Figure 3k) following the pattern of negative SAT anomalies (compare with Figure 3b). The −1.5 standard deviation level is about −4°C for Europe and China and −7°C for the central Siberia. These values are well comparable to the observed cold extremes discussed in our paper.

[21] The results described above suggest that SIC change in the B-K seas can exert a marked impact on local and remote atmospheric circulation and lead to SAT and circulation response similar to that observed, e.g., during the extremely cold winter 2005–2006. The revealed anomalous atmospheric circulation patterns, both in the troposphere and stratosphere, can distinctly differ from those attributed to NAO/AO variability.

4. Physical Mechanisms of the Remote and Local Atmospheric Responses to the Change in the B-K Sea Ice Concentration

[22] In general, the atmospheric circulation adjustment to a localized surface heat source is a product of complicated interplay between local (convective and baroclinic) and remote (mostly barotropic) responses [*Murray and Simmonds*, 1995; *Peng et al.*, 1997; *Walter et al.*, 2001; *Alexander et al.*, 2004]. The patterns of remote teleconnections shown in Figure 3 result from excitation of the large-scale quasi-barotropic Rossby waves in the vicinity of the Polar Jet as a response to considered variations of SIC, which is in line, specifically, with findings reported in the study by *Honda et al.* [2009] [see also *Alexander et al.*, 2004; *Deser et al.*, 2004].

[23] Meanwhile, as already indicated in section 3, the revealed local anomalous cyclone/anticyclone-type atmospheric response to the SIC changes in the B-K sector is the original pacemaker for a whole NH atmospheric circulation rearrangement. In particular, the above mentioned local anticyclonic anomalous circulation caused by the 80% to 40% SIC reduction brings about an eastward turn around the pole of the canonical negative NAO pattern (Figures 3b, 3e, and 3h) and modifies the classical negative AO structure aloft (Figures 4b, 4e, 4h, and 4k), note also the "hot spot" over the B-K sector that is completely unusual for SAT changes associated with negative NAO.
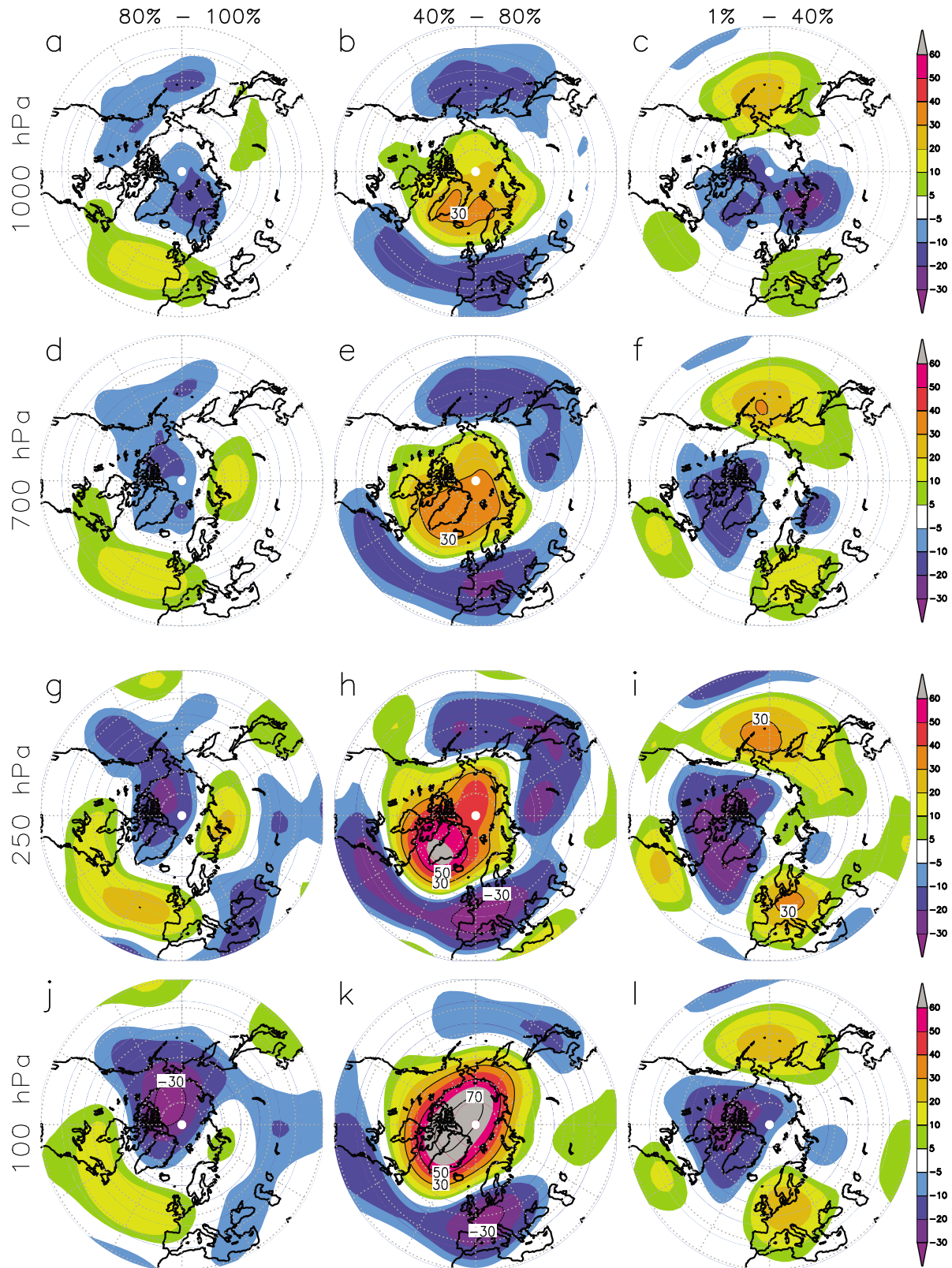
Figure 4. Change in the geopotential height (hpm) at (a–c) 1000 hPa, (d–f) 700 hPa, (g–i) 250 hPa, and (j–l) 100 hPa pressure levels as response to Barents-Kara sea ice transitions (as in Figure 3) from 100% to 80%, 80% to 40%, and 40% to 1% for February.

[24] One of the most interesting features of our simulations is a strong nonlinearity of the local atmospheric circulation response to SIC changes. In the following section, we present a brief description of the conceptual semi-analytical model that may explain the local nonlinear response and illustrate a possible physical mechanism. It is assumed that SIC reduction lead to interaction between basic diabatic processes within the atmospheric planetary boundary layer (PBL), namely, (1) anomalous heating of the lower troposphere because of the enhanced vertical turbulent heat flux at the surface; (2) increase in baroclinicity of the lower troposphere, owing to rise of the horizontal temperature gradients between the interior of the B-K sector and its periphery; and (3) variation of the near-surface cross-isobar angle that is generally determined by changes in surface friction and stratification of the PBL [*Hansen et al.*, 1983].

5. A Conceptual Model for the Local Atmospheric Response to the Change in the B-K Sea Ice Concentration

[25] To reveal a background physical mechanism for the nonlinear local response of atmospheric circulation to the decrease in SIC, we developed a conceptual model of response of the local lower troposphere to a heating source (the B-K sector in our case) at the lower boundary. For that purpose, we elaborated on the classical Wiin-Nielsen [*Wiin-Nielsen*, 1974] model of the baroclinic PBL. In this latter model, the vertical velocity w_h in the vicinity of the top h of the PBL reads

$$w_h \approx h\varsigma_{g0} \sin \alpha_0 \cos \alpha_0 - \frac{h^2 |\vec{V}_T|}{2^{1/2}} \frac{\varsigma_{g0}}{|\vec{V}_{g0}|} \sin(\alpha_T - \alpha_0) \cos\left(\frac{\pi}{4} + \alpha_0\right). \tag{1}$$

In (1), $|\vec{V}_{g0}|$ and $|\vec{V}_T|$ are, respectively, the absolute values of the near-surface geostrophic wind $\vec{V}_{g0}$ and the thermal wind $\vec{V}_T$; ς_{g0} is the near-surface geostrophic vorticity; α_0 is the near-surface cross-isobar angle (counted from $\vec{V}_{g0}$) between $\vec{V}_{g0}$ and the vector of the near-surface velocity $\vec{V}_0$, whereas $h = C_0 (2K_M/f_0)^{1/2}$ [*Charney and Eliassen*, 1949], where f_0 is the Coriolis parameter, K_M is the vertical coefficient of turbulent diffusivity, and C_0 is a dimensionless constant of order 1. The α_T term in (1) denotes the angle (counted from $\vec{V}_{g0}$) between $\vec{V}_T$ and $\vec{V}_{g0}$, and $\vec{V}_T$ is assumed to be constant in the PBL.

[26] Further, we diagnose the vertical velocity w_h in the left-hand side (LHS) of (1) from the thermodynamic energy equation as follows [*Holton*, 2004]:

$$w_h \approx \frac{1}{\rho_h \theta_h} \left[-\frac{\partial}{\partial t} \int_0^h \rho\theta \, dz - \int_0^h \nabla \cdot \rho\theta\vec{V} \, dz + \frac{F_s}{c_p} \right], \tag{2}$$

where c_p is the specific heat at constant pressure; ∇ is the horizontal gradient operator; ρ and θ are, respectively, the air density and the potential temperature with the corresponding values ρ_h and θ_h at $z \approx h$; $\vec{V}$ is the vector of the total horizontal velocity; and F_s stands for the diabatic sources/sinks in the PBL. Following a conventional assumption [e.g., *Hansen et al.*, 1983] F_s in (2) is thought of as the vertical heat flux

at the surface because of small/mesoscale turbulence and convection. Aiming at the interpretation of the presented in our paper results, which are 100 year averages for the corresponding ECHAM5 100 year runs, we omit the nonstationary term in the right-hand side (RHS) of (2). Then elimination of w_h between (1) and (2) yields

$$\frac{F_s}{c_p} - \int_0^h \nabla \cdot \rho\theta\vec{V} \, dz \approx \rho_h \theta_h \left[h\varsigma_{g0} \sin \alpha_0 \cos \alpha_0 - \frac{h^2 |\vec{V}_T|}{2^{1/2}} \frac{\varsigma_{g0}}{|\vec{V}_{g0}|} \sin(\alpha_T - \alpha_0) \cos\left(\frac{\pi}{4} + \alpha_0\right) \right]. \tag{3}$$

Equation (3) is the basic equation of our conceptual model that we use for calculation of ς_{g0} and corresponding pressure anomaly in the PBL. Starting from (3), using an assumption on a circular symmetry of the local atmospheric circulation response to a heating source and applying a parabolic approximation for radial distributions of near-surface temperature and pressure anomaly, one can express, after scale analysis and neglecting second-order terms, the surface pressure anomaly averaged over the B-K region, p_s, in terms of the dynamical and thermodynamical parameters of the heating region as follows (see Appendix A for details):

$$p_s \approx -\frac{f_0}{8h} \frac{<F_s> r_0^2}{c_p\theta_h <\sin\alpha_0><\cos\alpha_0>} + \frac{\rho^* h}{4} \frac{g}{\theta^*} \theta_c \left(1 - \frac{<\sin\alpha_0>}{<\cos\alpha_0>}\right). \tag{4}$$

In (4), g is the acceleration due to gravity, θ^* and ρ^* are accordingly the reference potential temperature and air density at $z = 0$, θ_c denotes the near-surface potential temperature difference between the deep interior of the "hot spot" and the environment taken with the opposite sign, while r_0 represents the characteristic linear scale (characteristic radius) of the "hot spot," and the angular brackets designate averaging over the heating area. The first term in the RHS of (4) is proportional to $\langle F_s \rangle$. The latter is a measure for the strength of those diabatic processes in the PBL favoring upward (convective-type) vertical motions and inducing the corresponding low-level positive cyclone-type vorticity and negative surface pressure anomaly p_s in (4). The magnitude of the first term depends also on the near-surface cross-isobar angle α_0 that represents the frictional processes in the PBL. The second term in the right side of (4) is proportional to θ_c that is a measure for the horizontal temperature gradients between the interior of the "hot spot" and its environment, driving the baroclinic-type horizontal advection within the PBL in the vicinity of the heating area. Depending on the magnitude and sign of θ_c (in our case, the latter is always negative) and the strength of the surface friction in terms of the near-surface cross-isobar angle α_0, the second term in the RHS of (4) can trigger, in accordance with its sign and magnitude relative to the first term, both anticyclone-type and cyclone-type overall atmospheric response in the PBL.

[27] Figure 5 demonstrates the dependence of p_s on SIC in the B-K sector calculated from the equation (4), using $\langle F_s \rangle$, T_c, and α_0 derived from the results of the ECHAM5 simulations, in comparison with the corresponding sea level pressure anomalies in the ECHAM5 runs. As can be seen
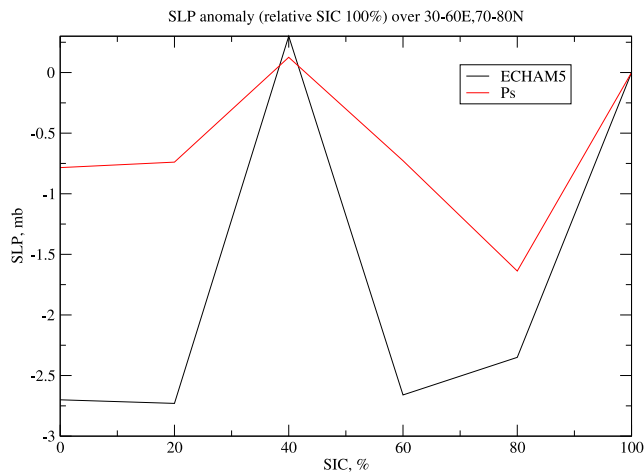
Figure 5. The B-K sector average sea level pressure anomaly (in hPa) corresponding to different values of the Barents-Kara sea ice concentration (SIC, in %) relative to that with 100% SIC, calculated from the conceptual semianalytical model (red) and computed from the ECHAM5 simulations (black).

from Figure 5, $p_s(80\%)$–$p_s(100\%)$, $p_s(40\%)$–$p_s(80\%)$, and $p_s(1\%)$–$p_s(40\%)$ are qualitatively (partly also quantatively) in line with the results of our ECHAM5 runs. As the environmental pressure p_e does not differ much in all six ECHAM5 simulations, the values of $p_s(80\%)$–$p_s(100\%)$, $p_s(40\%)$–$p_s(80\%)$, and $p_s(1\%)$–$p_s(40\%)$ from Figure 5 can be directly compared with the corresponding geopotential height anomalies (multiplied by ρg) in the neighborhood of the heat source shown in Figures 3g–3i. This comparison supports the hypothesis that the nonlinear response of the local lower troposphere circulation to SIC decline can be qualitatively and to some extent even quantitatively explained by the revealed in our conceptual model nonlinear interplay between "convective-frictional" and "baroclinic-frictional" mechanisms described above.

6. Discussion and Conclusions

[28] Significant implication of our work for climate change studies can be an important role of the B-K sea ice as an internal parameter regulating abrupt nonlinear transitions between different regimes of the atmospheric circulation in the sub-polar and polar regions of the NH. Our results suggest that large-scale easterlies accompanying an anticyclone-type vortex over the heating source dominate quasi-zonal anomaly pattern in the subpolar latitudes caused by 80% to 40% SIC reduction (Figures 3b, 3e, and 3h), whereas meridional-type responses with cyclonic circulations above the heating source and anticyclonic vortices in midlatitudes prevail in the cases of 100% to 80% and 40% to 1% SIC decrease. We show that the revealed nonlinear local response to sea ice decrease may stem from interplay between convectional-frictional (because of the anomalous diabatic warming over the "hot spot" and change in the surface friction conditions) and baroclinic-frictional (due to modified temperature gradients in the neighborhood of the heat source and change in the surface friction force) mechanisms of the lower atmosphere response to SIC changes.

[29] The presented mechanism does not, of course, determine an overall SAT variability in the northern high latitudes in wintertime [*Semenov and Bengtsson*, 2003] which is dominated by the NAO [*Hurrell*, 1995; *Magnusdottir et al.*, 2004; *Deser et al.*, 2004] and other major variability modes like ENSO [*Fraedrich and Müller*, 1992; *Merkel and Latif*, 2002; *Brönnimann et al.*, 2004] and Atlantic multidecadal SST changes [*Sutton and Hodson*, 2007; *Semenov et al.*, 2010]. In particular, a contribution from the Atlantic Ocean's temperature anomalies and anomalous stratospheric circulation [*Scaife and Knight*, 2008], as well as cloud-diabatic effects [*Croci-Maspoli and Davies*, 2009], could be important in producing unusually cool winter temperatures like those observed in 2005–2006. Also, the wintertime sea ice variations in the Arctic are generally linked to the NAO [*Dickson et al.*, 2000; *Deser et al.*, 2000]. However, as demonstrated here, the change in the B-K SIC can be an important link in the chain of feedbacks governing the atmospheric circulation realignment over the northern continents and Polar Ocean. Moreover, a link between NAO and Arctic sea ice is not stationary [*Semenov*, 2008], and considerable sea ice changes may happen unrelated to the NAO variability [*Deser and Teng*, 2007]. Thus, the mechanism suggested in our paper may markedly contribute to the major SAT variability modes in the years of weak ENSO and NAO. It may also bring about powerful feedbacks to atmospheric circulation from corresponding sea ice changes, in line with other modeling results [e.g., *Alexander et al.*, 2004; *Deser et al.*, 2004].

[30] An important result of our simulations is that a decrease of the wintertime sea ice cover in the Barents and Kara seas does not always result in a priori expected warming over the adjacent continental areas. A robust cooling may also be associated with the sea ice reduction within a certain range, which can be important in perspective of global climate change. This issue can be specifically interesting in light of the observed long-term positive NAO tendency [*Kodera et al.*, 1999; *Gulev et al.*, 2002] that may be partly induced by the anthropogenic greenhouse gas forcing [e.g., *Ulbrich and Christoph*, 1999]. As pointed out in the studies by *Gulev et al.* [2002] and *Ulbrich and Christoph* [1999], the associated change in the storm track activity over the North Atlantic is quite noticeable. This can be related to a systematic northeastward shift of the NAO variability pattern. In context of our study, the positive trend of NAO index and northeastward shift of the NAO variability pattern could favor a decreased sea ice cover over the B-K sector that, in turn, might impose negative feedback on the SAT response, unless SIC would become very low. On the other hand, the observed northeastward shift per se of the lower-tropospheric NAO pattern could, to some extent, be favored by the decrease in SIC, as discussed above in section 3.

Appendix A

[31] For simplicity, we can admit a circular horizontal geometry of the lower atmosphere parameters in the vicinity of heating region (the B-K sector) with isobars and isotherms represented by the concentric circles. This is in general in line with the geographical distributions for the corresponding variables pictured by Figure 3. For the circular symmetry of the isobars and isotherms, $\vec{V}_T$ and $\vec{V}_{g0}$ are

either collinear that gives $\alpha_T = 0$, or anticollinear, with $\alpha_T = \pi$ [*Wiin-Nielsen*, 1974]. On the basis of the observational data [e.g., *Sorteberg and Kvingedal*, 2006], the background lower-troposphere flow, the latter we attribute to the case of 100% SIC with $F_s \approx 0$ and $\vec{V}_T \approx 0$, is supposed to possess a close-to-zero vorticity. Under the above mentioned assumptions the second term in the LHS of (3) yields

$$-\int_0^h \nabla \cdot \rho\theta\vec{V}\,dz \approx -\int_0^h \nabla \cdot \rho\theta\vec{V}_{ag}\,dz, \tag{A1}$$

where $\vec{V}_{ag}$ is the ageostrophic wind within the PBL. Then (3) holds after division by $\rho_h\theta_h$

$$\frac{F_s}{c_p\rho_h\theta_h} - \frac{1}{\rho_h\theta_h}\int_0^h \nabla\rho\theta\vec{V}_{ag}\,dz \approx h\varsigma_{g0}\left[\sin\alpha_0\cos\alpha_0\right.$$
$$\left. - \frac{h|\vec{V}_T|}{2^{1/2}|\vec{V}_{g0}|}\sin(\alpha_T - \alpha_0)\cos\left(\frac{\pi}{4} + \alpha_0\right)\right]. \tag{A2}$$

Turning into cylindrical system of coordinates (r, φ, z), equation (A2) reads

$$\frac{F_s}{c_p}\rho_h\theta_h - \frac{1}{\rho_h\theta_h}\int_0^h \nabla_r\rho\theta\vec{V}_{agr}\,dz \approx h\frac{1}{\rho^*f_0}\frac{1}{r}\frac{\partial}{\partial r}\left(r\frac{\partial p_0}{\partial r}\right)$$
$$\cdot\left[\sin\alpha_0\cos\alpha_0 - \frac{h}{2}\left|\frac{g}{f_0\theta^*}\frac{\partial\theta_0}{\partial r}\right|\left|\frac{1}{\rho^*f_0}\frac{\partial p_0}{\partial r}\right|^{-1}\right.$$
$$\left. \cdot\sin(\alpha_T - \alpha_0)(\cos\alpha_0 - \sin\alpha_0)\right]. \tag{A3}$$

In (A3), g is the acceleration due to gravity; ∇_r and $\vec{V}_{agr}$ are accordingly the radial components of the vectors ∇ and $\vec{V}_{ag}$; θ^* and ρ^* are, correspondingly, the reference temperature and air density at $z = 0$, whereas p_0 and θ_0 are, respectively, the near-surface pressure and potential temperature over the "hot spot," with r_0 denoting its characteristic linear spatial scale (characteristic radius).

[32] It is instructive to reveal the specific features of equation (A3) using simple but realistic geographical distributions of p_0 and θ_0 within and in close vicinity of the B-K sector

$$p_0 = (p_e - p_c) + p_c(r/r_0)^2 \tag{A4}$$

$$\theta_0 = (\theta_e - \theta_c) + \theta_c(r/r_0)^2 \tag{A5}$$

for $0 \le r < r_0$, where r_0 is the characteristic length scale (radius) of the B-K sector, with the prescribed environmental parameters p_e and θ_e. This way, $p_c > 0$ ($p_c < 0$) in (A4) corresponds to a cyclone (anticyclone) distribution for the near-surface pressure within the sector.

[33] After applying approximations (A4) and (A5) for the variables $\frac{1}{\rho^*f_0}\frac{1}{r}\frac{\partial}{\partial r}\left(r\frac{\partial p_0}{\partial r}\right)[= \varsigma_{g0}]$, $\left|\frac{1}{\rho^*f_0}\frac{\partial p_0}{\partial r}\right|[= |\vec{V}_{g0}|]$ and $\left|\frac{g}{f_0\theta}\frac{\partial\theta_0}{\partial r}\right|[= |\vec{V}_T|]$ entering (A3), one gets

$$\frac{1}{\rho^*f_0}\frac{1}{r}\frac{\partial}{\partial r}\left(r\frac{\partial p_0}{\partial r}\right) = \frac{4p_c}{\rho^*f_0 r_0^2} \tag{A6}$$

$$\left|\frac{1}{\rho^*f_0}\frac{\partial p_0}{\partial r}\right| = \frac{2|p_c|}{\rho^*f_0}\frac{r}{r_0^2} \tag{A7}$$

$$\left|\frac{g}{f_0\theta^*}\frac{\partial\theta_0}{\partial r}\right| = \frac{2g|\theta_c|}{f_0\theta^*}\frac{r}{r_0^2}. \tag{A8}$$

We can compare the magnitudes of the first and second terms in the LHS of (A3) using the first-order approximation $|\vec{V}_{ag}| \approx |\vec{V}_{g0}|\sin\alpha_0$ [*Wiin-Nielsen*, 1974], where $|\vec{V}_{g0}|$ equals the LHS of (A7). Integration of the LHS of (A3) with respect to r and φ yields, for $0 \le r < r_0$

$$\int_0^r\int_0^{2\pi}\frac{F_s}{c_p\rho_h\theta_h}r\,d\varphi\,dr \approx \frac{\langle F_s\rangle_r}{c_p\rho_h\theta_h}\pi r^2 \tag{A9}$$

$$\int_0^r\int_0^{2\pi}\frac{1}{\rho_h\theta_h}\int_0^h\nabla_x\rho\theta\vec{V}_{agr}\,dz\,r\,d\varphi\,dr \le \frac{4\pi h|p_c|r^2}{\rho_k f_0 r_0^2}\langle\sin\alpha_0\rangle_r, \tag{A10}$$

where $\langle F_s\rangle_r$ and $\langle\sin\alpha_0\rangle_r$ are correspondingly F_s and $\sin\alpha_0$ averaged over the area of a circle with the radius r. In the considered ECHAM5 simulations, $\langle F_s\rangle_{r0}$ and $|p_c|$ are, respectively, of order $O(100 \text{ W m}^{-2})$ and $O(50 \text{ Pa})$ in the B-K sector. Then, with $\theta_h \approx 273$ K, $f_0 \approx 1.46 \times 10^{-4}$ s^{-1}, $h \approx 10^2$ m, $r_0 \approx 1.5 \times 10^6$ m, and $\langle\sin\alpha_0\rangle_r \approx 0.5$, we obtain from (A9) and (A10) that the characteristic magnitude for the ratio of the second to the first term in the LHS of (A3) is not larger than $4c_p h_f\theta_h|p_c|\langle\sin\alpha_0\rangle_{r0}/f_0 r_0^2\langle F_s\rangle_{r0}$, the latter being of the order of $O(10^{-1})$. Hence, to a first approximation, we can neglect the second term in the LHS of (A3). This reduces (A3), with (A6)–(A8) taken into account, to the following equation (hereafter $\langle Y\rangle$ denotes $\langle Y\rangle_{r0}$, for any Y):

$$\frac{\langle F_s\rangle}{c_p\rho_h\theta_h} \approx h\frac{4p_c}{\rho^* f_0 r_0^2}\left[\langle\sin\alpha_0\rangle\langle\cos\alpha_0\rangle - h\frac{g|\theta_c|}{\theta^*}\left[\frac{2|p_c|}{\rho^*}\right]^{-1}\right.$$
$$\left. \cdot\langle\sin(\alpha_T - \alpha_0)\rangle(\langle\cos\alpha_0\rangle - \langle\sin\alpha_0\rangle)\right]. \tag{A11}$$

Solving (A11) for p_c, one gets (in both cases of collinear (with $\alpha_T = 0$) and anticollinear (with $\alpha_T = \pi$) $\vec{V}_{g0}$ and $\vec{V}_T$) the following expression:

$$p_c \approx \frac{f_0}{4h}\frac{\langle F_s\rangle r_0^2\rho^*}{c_p\rho_h\theta_h\langle\sin\alpha_0\rangle\langle\cos\alpha_0\rangle} - \frac{\rho^* h}{2}\frac{g}{\theta^*}\theta_c\left(1 - \frac{\langle\sin\alpha_0\rangle}{\langle\cos\alpha_0\rangle}\right). \tag{A12}$$

The prescribed parameters in the equation (A12) are assigned to the following values: $\rho_h \approx \rho^* \approx 1.29$ kg/m^3, $\theta_h \approx \theta^* \approx 273$ K, $c_p = 1 \times 10^3$ J kg^{-1} K^{-1}, $g = 10$ m s^{-2}, $r_0 \approx 1.5 \times 10^6$ m, $f_0 = 1.46 \times 10^{-4}$ s^{-1}, $K_M \approx 5$ m^2 s^{-1}, and $C_0 = 2.5$ in the equation for h. After averaging $p_0 - p_e$ over the heating area with the radius r_0 using (A4), one gets for the averaged surface pressure anomaly, $p_s = \langle p_0 - p_e\rangle$:

$$p_s = -p_c/2 \approx -\frac{f_0}{8h}\frac{\langle F_s\rangle r_0^2\rho^*}{c_p\rho_h\theta_h\langle\sin\alpha_0\rangle\langle\cos\alpha_0\rangle}$$
$$+ \frac{\rho^* h}{4}\frac{g}{\theta^*}\theta_c\left(1 - \frac{\langle\sin\alpha_0\rangle}{\langle\cos\alpha_0\rangle}\right) \tag{A13}$$

which is equation (4) in the main body of the paper.

References

Alexander, M. A., U. S. Bhatt, J. E. Walsh, M. S. Timlin, J. S. Miller, and J. D. Scott (2004), The atmospheric response to realistic Arctic sea ice anomalies in an AGCM during winter, *J. Clim.*, 17, 890–905.

Bengtsson, L., V. A. Semenov, and O. M. Johannessen (2004), The early twentieth-century warming in the Arctic—A possible mechanism, *J. Clim.*, 17, 4045–4057.

Baldwin, M. P, and T. J. Dunkerton (2001), Stratospheric harbingers of anomalous weather regimes, *Science*, 294, 581–584.

Brönnimann, S., J. Luterbacher, J. Staehelin, T. M. Svendby, G. Hansen, and T. Svenøe (2004), Extreme climate of the global troposphere and stratosphere 1940–1942 related to El Niño, *Nature*, 431, 971–974.

Calov, R., A. Ganopolski, M. Claussen, V. Petoukhov, and R. Greve (2005a), Transient simulation of the last glacial inception. Part I: Glacial inception as a bifurcation in the climate system, *Clim. Dyn.*, 24, 545–561.

Calov, R., A. Ganopolski, M. Claussen, V. Petoukhov, and R. Greve (2005b), Transient simulation of the last glacial inception. Part II: Sensitivity and feedback analysis, *Clim. Dyn.*, 24, 563–576.

Cavalieri, D., C. Parkinson, P. Gloersen, and H. J. Zwally (1996), Sea ice concentrations from Nimbus-7 SMMR and DMSP SSM/I passive microwave data, National Snow and Ice Data Center, Boulder Colo, USA, Digital media. (Available at http://nsidc.org/data/nsidc-0051.html)

Charney, J. G., and A. Eliassen (1949), A numerical method for predicting the perturbation of the middle latitude westerlies, *Tellus*, 1, 38–54.

Cohen, J., M. Barlow, P. J. Kushner, and K. Saito (2007), Stratosphere-troposphere coupling and links with Eurasian land surface variability, *J. Clim.*, 20, 5335–5343.

Croci-Maspoli, M., and H. C. Davies (2009), Key dynamical features of the 2005/06 European winter, *Mon. Weather Rev.*, 137, 664–678.

Deser, C., J. E. Walsh, and M. S. Timlin (2000), Arctic sea ice variability in the context of recent atmospheric circulation trends, *J. Clim.*, 13, 617–633.

Deser, C., G. Magnusdottir, R. Saravanan, and A. Phillips (2004), The effects of North Atlantic SST and sea ice anomalies on the winter circulation in CCM3. Part II: Direct and indirect components of the response, *J. Clim.*, 17, 877–889.

Deser, C., and H. Teng (2007), Evolution of Arctic sea ice concentration trends and the role of atmospheric circulation forcing, 1979–2007, *Geophys. Res. Lett.*, 35, L02504, doi:10.1029/2007GL032023.

Diaz, H., and V. Markgraf (Eds) (2000), *El Niño and the Southern Oscillation: Multiscale Variability and Global and Regional Impacts*, Cambridge Univ. Press, Cambridge, U. K.

Dickson, R. R., et al. (2000), The Arctic Ocean response to the North Atlantic oscillation, *J. Clim.*, 13, 2671–2696.

Gulev, S. K., T. Jung, and E. Ruprecht (2002), Climatology and interannual variability in the intensity of synoptic-scale processes in the North Atlantic from the NCEP-NCAR reanalysis data, *J. Clim.*, 15, 809–828.

Fraedrich, K., and K. Müller (1992), Climate anomalies in Europe associated with ENSO extremes, *Int. J. Climatol.*, 12, 25–31.

Hansen, J., et al. (1983), Efficient three-dimensional global models for climate studies: Models I and II, *Mon. Weather Rev.*, 111, 609–662.

Herman, G. F., and W. T. Johnson (1978), The sensitivity of the general circulation to Arctic sea ice boundaries: A numerical experiment, *Mon. Weather Rev.*, 106, 1649–1663.

Holton, J. R. (2004), *An Introduction to Dynamic Meteorology*, 4th Edition, Academic Press, Oxford, U. K.

Honda, M., J. Inoue, and S. Yamane (2009), Influence of low Arctic sea-ice minima on wintertime Eurasian coldness, *Geophys. Res. Lett.*, 36, L08707, doi:10.1029/2008GL037079.

Hurrell, J. W. (1995), Decadal trends in the North Atlantic Oscillation: Regional temperatures and precipitation, *Science*, 269, 676–679.

Hurrell, J. W., et al. (2008), A new sea surface temperature and sea ice boundary data set for the Community Atmosphere Model, *J. Clim.*, 21, 5145–5153.

Kalnay, E., et al. (1996), The NCEP/NCAR 40 year reanalysis project, *Bull. Am. Meteorol. Soc.*, 77, 437–470.

Kodera, K., H. Koide, and H. Yoshimura (1999), Northern Hemisphere winter circulation associated with the North Atlantic Oscillation and stratospheric polar-night jet, *Geophys. Res. Lett.*, 26, 443–446, doi:10.1029/1999GL900016.

Magnusdottir, G., C. Deser, and R. Saravanan (2004), The effects of North Atlantic SST and sea ice anomalies on the winter circulation in CCM3.

Part I: Main features and storm track characteristics of the response, *J. Clim.*, 17, 857–876.

Merkel, U., and M. Latif (2002), A high resolution AGCM study of the El Niño impact on the North Atlantic/European sector, *Geophys. Res. Lett.*, 29(9), 1291, doi:10.1029/2001GL013726.

Murray, R. J., and I. Simmonds (1995), Responses of climate and cyclones to reductions in Arctic winter sea ice, *J. Geophys. Res.*, 100, 4791–4806, doi:10.1029/94JC02206.

NOAA (2010), Climate Prediction Center (Available at http://www.cpc.noaa.gov/data/indices/)

Osborn, T. J. (2006), Recent variations in the winter North Atlantic Oscillation, *Weather*, 61, 353–355.

Parkinson, C. L., D. J. Cavalieri, P. Gloersen, H. J. Zwally, and J. C. Comiso (1999), Arctic sea ice extents, areas, and trends, 1978–1996, *J. Geophys. Res.*, 104, 20837–20856, doi:10.1029/1999JC900082.

Peng, S., W. A. Robinson, and M. P. Hoerling (1997), The modeled atmospheric response to midlatitude SST anomalies and its dependence on background circulation states, *J. Clim.*, 10, 971–987.

Philipona, R., B. Durr, A. Ohmura, and C. Ruckstuhl (2005), Anthropogenic greenhouse forcing and strong water vapor feedback increase temperature in Europe, *Geophys. Res. Lett.*, 32, L19809, doi:10.1029/2005GL023624.

Polyakov, I. V., et al. (2002), Observationally based assessment of polar amplification of global warming, *Geophys. Res. Lett.*, 29(18), 1878, doi:10.1029/2001GL011111.

Roeckner, E., et al. (2003), The atmospheric general circulation model ECHAM5. Part I: Model description, *Rep. 349*, Max Planck Inst. for Meteorol., Hamburg, Germany.

Scaife, A. A., and J. R. Knight (2008), Ensemble simulations of the cold European winter of 2005–2006, *Q. J. R. Meteorol. Soc.*, 134, 1647–1659, doi:10.1002/qj.312.

Seierstad, I. A., and J. Bader (2009), Impact of a projected future Arctic Sea Ice reduction on extratropical storminess and the NAO, *Clim. Dyn.*, 33, 937–943, doi:10.1007/s00382-008-0463-x.

Semenov, V. A. (2008), Influence of oceanic inflow to the Barents Sea on climate variability in the Arctic region, *Doklady Earth Sci.*, 418, 91–94.

Semenov, V. A., and L. Bengtsson (2003), Modes of the wintertime Arctic temperature variability, *Geophys. Res. Lett.*, 30(15), 1781, doi:10.1029/2003GL017112.

Semenov, V. A., M. Latif, D. Dommenget, N. S. Keenlyside, S. Strehz, T. Martin, and W. Park (2010), The impact of North Atlantic-Arctic multidecadal variability on Northern Hemisphere surface air temperature, *J. Clim.*, 23, 5668–5677.

Serreze, M. C., and J. Francis (2006), The Arctic amplification debate, *Clim. Change*, 76, 241–264, doi:10.10007/s10584-005-9017.

Singarayer, J. S., J. L. Bamber, and P. J. Valdes (2006), Twenty-first century climate impacts from a declining Arctic sea ice cover, *J. Clim.*, 19, 1109–1125.

Sorteberg, A., and B. Kvingedal (2006), Atmospheric forcing on the Barents sea winter ice extent, *J. Clim.*, 19, 4772–4784.

Stroeve, J., M. M. Holland, W. Meier, T. Scambos, and M. Serreze (2007), Arctic sea ice decline: Faster than forecast, *Geophys. Res. Lett.*, 34, L09501, doi:10.1029/2007GL029703.

Sutton, R. T., and D. L. Hodson (2007), Climate response to basin-scale warming and cooling of the North Atlantic Ocean, *J. Clim.*, 20, 891–907.

Takaya, K., and H. Nakamura (2005), Mechanisms of intraseasonal amplification of the cold siberian high, *J. Atmos. Sci.*, 62, 4423–4440.

Takaya, K., and H. Nakamura (2008), Precursory changes in planetary wave activity for midwinter surface pressure anomalies over the Arctic, *J. Meteorol. Soc. Jpn*, 86, 415–427.

Thompson, D. W., and J. M. Wallace (1998), The arctic oscillation signature in the wintertime geopotential height and temperature fields, *Geophys. Res. Lett.*, 25, 1297–1300, doi:10.1029/98GL00950.

Ulbrich, U., and M. Christoph (1999), A shift of the NAO and increasing storm track activity over Europe due to anthropogenic gas forcing, *Clim. Dyn.*, 15, 551–559.

Walter, K., U. Luksch, and K. Fraedrich (2001), A response climatology of idealized midlatitude thermal forcing experiments with and without a storm track, *J. Clim.*, 14, 467–484.

Wiin-Nielsen, A. (1974), Vorticity, divergence, and vertical velocity in a baroclinic boundary layer with a linear variation of the geostrophic wind, *Bound. Layer Meteorol.*, 6, 459–476.

V. Petoukhov, Potsdam-Institute for Climate Impact Research, Telegrafenberg A62/PO Box 60 12 03, D-14473/14412 Potsdam, Germany. (petukhov@pik-potsdam.de)

V. A. Semenov, Leibniz Institute of Marine Sciences at the University of Kiel, Duesternbrooker Weg 20, D-24105 Kiel, Germany.